

Interplay of Thermal and Electronic Effects in the Mott Transition of Nanosized VO₂ Phase Change Memory Devices

László Pósa,* Péter Hornung, Tímea Nóra Török, Sebastian Werner Schmid, Sadaf Arjmandabasi, György Molnár, Zsófia Baji, Goran Dražić, András Halbritter, and János Volk



Cite This: <https://doi.org/10.1021/acsanm.3c00150>



Read Online

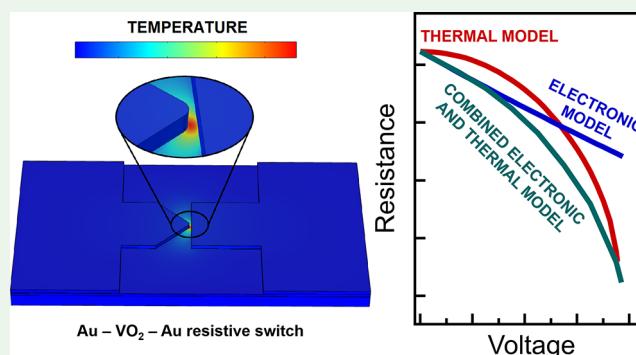
ACCESS |

Metrics & More

Article Recommendations

ABSTRACT: Volatile memory devices relying on the Mott-type insulator-to-metal transition of vanadium oxide (VO₂) are widely utilized in the field of neuromorphic computing. Such devices, however, are realized in a nanoscale geometry, where the switching relies on the self-heating of an ultrasmall spot as well as the presence of extremely high electric fields in the active region. In this paper, we investigate the interplay of such nanoscale thermal and nonlinear electronic phenomena by investigating the temperature and voltage dependent conduction properties of our custom-designed VO₂ devices, where a V-shaped electrode focuses the switching to an ultrasmall single-spot active region. This simplified spatial structure of the active volume facilitates the device modeling and the identification of physical mechanisms behind the phase transition. We find that purely thermal or electronic effects fail to describe the device operation, however, according to our finite element simulations, a combined electronic and thermal model provides a precise description of the device characteristics. These results facilitate the understanding as well as the thermal and electronic design of novel VO₂-based neuronal devices.

KEYWORDS: resistive switching memory, Mott transition, vanadium dioxide, transport mechanism, finite element simulation, focused active region



1. INTRODUCTION

VO₂ has been studied for decades due to its metal-insulator (MIT) transition at $T \approx 68$ °C. This first-order phase transition is accompanied by the structural transformation from low-temperature monoclinic to high-temperature tetragonal phase. Besides the structural and electronic properties, the optical features also change remarkably between the two phases. Due to the near room temperature phase transition, VO₂ is an attractive material for various applications including electromechanical devices, sensors and transistors.^{1–8} Recently, the advantageous properties of VO₂ were also exploited in the field of neuromorphic computing, taking advantage of the volatile resistive switching characteristics of VO₂ devices.^{9–16}

The latter resistive switching phenomenon is basically realized in lateral devices, where the initially poorly conducting VO₂ layer is contacted on the top by two metallic electrodes with a planar separation of ≈ 100 nm^{−1} μm. By the application of a proper voltage, the high electric field between the contacting electrodes together with the induced Joule heating trigger a local phase transition driving the device to a low resistance state (LRS). After releasing the voltage the device relaxes back to the original high resistance state (HRS). These volatile resistive switches exhibit excellent characteristics with

stable and reproducible operation up to 10⁹ cycles,¹⁷ and simple circuits including one or two VO₂ switches, capacitors, resistors, and batteries can realize artificial neurons that can mimic most of the known biological neuronal dynamic patterns.^{9,11,15,18,19} Alternatively, the underlying switching mechanism exhibits remarkable complexity both in the temporal and spatial domains. The former is reflected in the subthreshold switching characteristics for rapidly repeated programming pulses,¹⁰ whereas spatially an inhomogeneous switching region was discovered, where the formation of conductive regions is more pronounced at the device edges.^{20,21} The description of these phenomena requires complex modeling tools, like a percolation network model.^{20–23}

In this paper, we aim to lessen the complexity of the physical operation in VO₂ resistive switches by focusing the switching

Received: January 10, 2023

Accepted: May 11, 2023

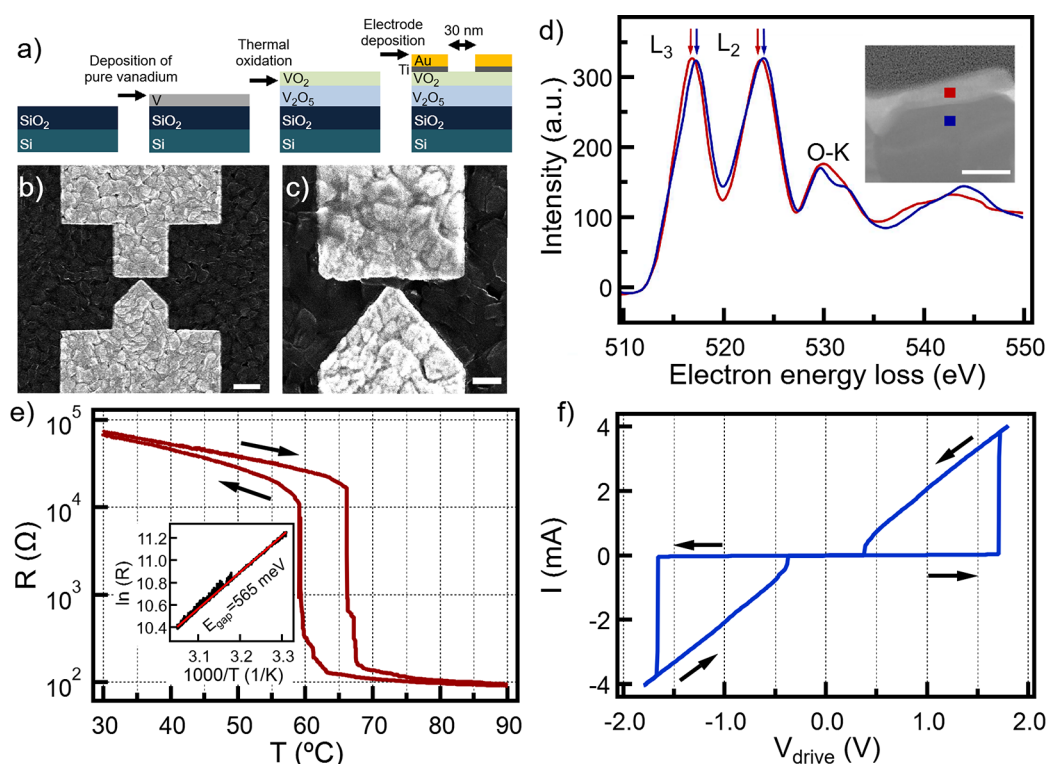


Figure 1. Device fabrication and characterization. a) Schematic, not to scale illustration of the adjacent fabrication steps of the nanosized VO_2 phase change memory devices. The cross-section is taken parallel to the nanogap axis. Scanning electron microscopy (SEM) image of the device before (b) and after (c) performing the electrical measurements. After the electrically induced switching cycles no substantial changes can be observed in the device structure. The scale bar in the initial b) SEM image indicates 500 nm, whereas in panel c) it indicates 200 nm. d) EELS spectra measured at different regions of the thermally oxidized vanadium-oxide layer. The inset shows the corresponding cross-sectional TEM image. The colored squares mark the position of the EELS measurements, the scale bar indicates 100 nm. e) Temperature dependent resistance shows very sharp phase transition, characteristic to VO_2 . The arrows indicate the direction of the hysteresis loop. The inset shows the $\ln(R)$ vs $1/T$ plot from the heating trace below T_c . The fitted line yields a 565 meV energy band gap in the semiconducting state. f) Switching $I(V)$ trace of the nanogap device. The device shows stable unipolar switching behavior. The switching direction is marked by the arrows.

to an even smaller and more well-defined active volume. To this end, we establish devices with an ultrasmall (≈ 30 nm) spacing between the contacting electrodes, and furthermore, the V-shaped arrangement of one of the electrodes focuses the switching into a well-defined spot.²⁴ Such nanosized VO_2 devices also exhibit highly stable switching characteristics, however, due to the ultrasmall focused active volume we anticipate that these devices are already describable by the formation and disappearance of a single metallic spot instead of more complex spatial patterns. This simplified arrangement facilitates the device modeling, providing further insight into the details of the local electronic and thermal processes. From this inspiration we perform a detailed investigation of the temperature and voltage dependent characteristics of the devices, analyze these in terms of model considerations, and finally compare our experimental observations to the results of finite element simulations relying on the realistic device geometry, and the available thermal transport parameters of the vanadium oxide layers. This analysis shows that purely thermal or electronic phenomena fail to describe the details of the resistive switching transition, however, the interplay of Joule heating with nonlinear electronic phenomena already provides a proper description of the observed device characteristics. Moreover, it reveals the relevant transport mechanism in the high resistance state.

2. RESULTS AND DISCUSSION

Our devices were fabricated in lateral arrangement by depositing Ti/Au metal electrodes onto a Si/SiO₂ substrate covered by a VO_x layer; the fabrication steps are illustrated in Figure 1a and more detailed description is available in the Methods. The gold top electrodes (light gray) were patterned by electron beam lithography, realizing an asymmetric structure with a triangular electrode on one side and a rectangular one on the other (see the SEM image in Figure 1b). At the narrowest spot (i.e., at the peak of the triangular electrode) the separation of the two electrodes is ≈ 30 nm. The VO_2 layer (dark gray) was produced by the thermal oxidation of a pure, 100 nm thick V layer.²⁵ The cross-section of the prepared oxide film was analyzed by transmission electron microscopy (TEM), showing two clearly distinguishable layers, a grainy and thicker dark gray layer at the bottom, which is covered by a thinner, light gray layer (see Figure 1c inset). The thickness of the film was found to expand to around 220 nm during the oxidation, which is consistent with the density and molar mass changes.²⁵ Electron energy loss spectroscopy (EELS)^{26–28} was also applied on these layers, indicating different oxidation states. The EELS spectrum of the bottom layer (blue line in Figure 1d and blue dot in the inset) is consistent with the V_2O_5 phase, whereas the top layer rather shows the presence of VO_2 (red line and dot in Figure 1d). The thickness of the top VO_2 film is not homogeneous, it varies in the range of $t_{\text{VO}_2} = 30\text{--}50$ nm. Accordingly, the

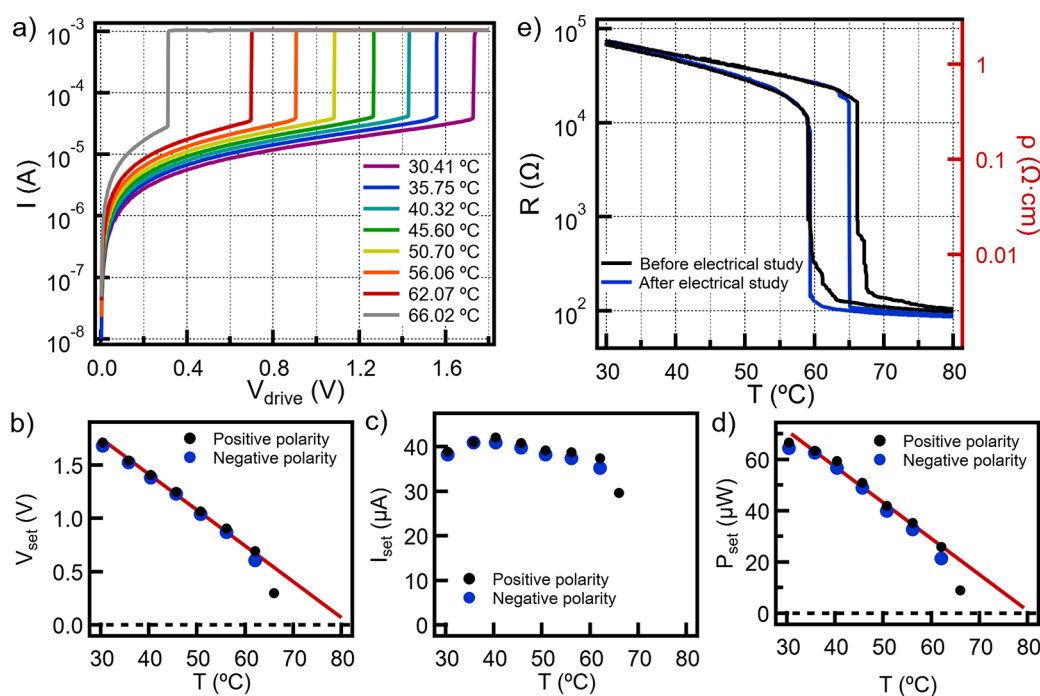


Figure 2. Influence of temperature on the switching mechanism. a) Current–voltage characteristics on logarithmic current scale recorded at different base temperatures. The resistive switching occurs at decreasing voltages as the temperature increases. b) Set voltage (V_{set}) as a function of the base temperature. The linear tendency is emphasized by a red guide to the eye line. c) Dependence of the set current (I_{set}) on the base temperature, showing nearly constant value. d) Switching power (P_{set}) versus temperature shows almost the same linear tendency as the V_{set} , highlighted by guide to the eye line. The black and blue dots in panels (b–d) refer to the values measured at positive and negative voltage polarity, respectively. All values, except the highest temperature, are calculated by averaging the set characteristics of ten cycles. The error bar is smaller than the size of the dots. e) Temperature dependent resistance before (black curve) and after (blue curve) the electrical study of the device. The characteristics of the semiconducting state did not change, only the phase change temperature slightly shifted to a lower value and the transition became more abrupt. The red axis on the right shows the corresponding resistivity value, the geometrical scaling factor between the resistance and resistivity was determined by finite element simulation.

thickness of the bottom V_2O_5 layer is around $t_{\text{V}_2\text{O}_5} = 180 \pm 10$ nm. See more details on the preparation and characterization of the VO_2 thin film in the [Methods](#).

The presence of VO_2 at the surface region is also supported by the temperature dependent electrical resistance measurement. The device shows pronounced phase change characteristic, shown in [Figure 1e](#). Below the phase transition temperature (T_c) the device exhibits semiconducting behavior with $E_{\text{gap}} = 565$ meV band gap energy (see inset), which is in good agreement with the literature values.^{29–31} By increasing the temperature the resistance drops suddenly at $T_c = 66.22$ °C, while the device transforms to the low resistance metallic state. The resistance switching ratio between 30 and 100 °C exceeds 600. We anticipate that the discrete jumps in the $R(T)$ curve during the transition are related to the involvement of only a few VO_2 grains in the electrical transport. Due to the hysteric behavior during the cooling process, the layer transforms back to the initial semiconductor phase at 7.2 °C lower temperature.

To electrically induce the phase transition we applied triangular voltage signals to the device with gradually increased amplitude at room temperature. The length of the triangular voltage sweep was chosen to 0.2 s with a repetition rate of 1 s to allow sufficiently long time for the structural relaxation of the VO_2 layer after the reset process and thus to minimize the effect of the subthreshold switching phenomenon.¹⁰ A serial resistor of $R_s = 380 \Omega$ was included in the circuit to limit the power dissipation in the low resistance state. The bias voltage

on the device is calculated as $V_{\text{bias}} = V_{\text{drive}} - I \cdot R_s$, the HRS resistance, however, is 2 orders of magnitude larger than R_s , that is, in the HRS $V_{\text{bias}} \approx V_{\text{drive}}$ applies. [Figure 1f](#) shows the first switching current–voltage ($I(V)$) characteristic, when the bias voltage on the sample exceeded the switching threshold value (V_{set}). The device switches abruptly from high to low resistance state (set process) at positive voltage polarity at $V_{\text{set}} = 1.71$ V and shows unipolar behavior, namely, the same switching characteristic is visible at the negative polarity. The switching cycles could be repeated 10^4 – 10^5 times, while the switching parameters showed high stability. The SEM images taken after the electrical operation do not reveal any substantial degradation in the active region (see [Figure 1c](#)). We have also studied the device-to-device variation using various VO_2 substrates as well as devices with various electrode separations in the 15–75 nm range. These reference measurements exhibit a clear increase of V_{set} with the electrode separation (see [Figure 6](#) in the [Methods](#)), which highlights the advantage of the ultrasmall devices with respect to the energy consumption.

In the following, we study the scaling of the switching parameters as well as the detailed evolution of the device resistance with the base temperature and bias voltage with the goal of identifying the contribution of the thermal and electronic effects in the device operation, focusing on samples with ≈ 30 nm electrode separation. [Figure 2a](#) shows $I(V)$ characteristics recorded at different temperatures between 30.4 and 66 °C. For better clarity only the upward voltage sweeps are plotted and for better current resolution high amplification was used, thereby the current could be resolved until 1 mA

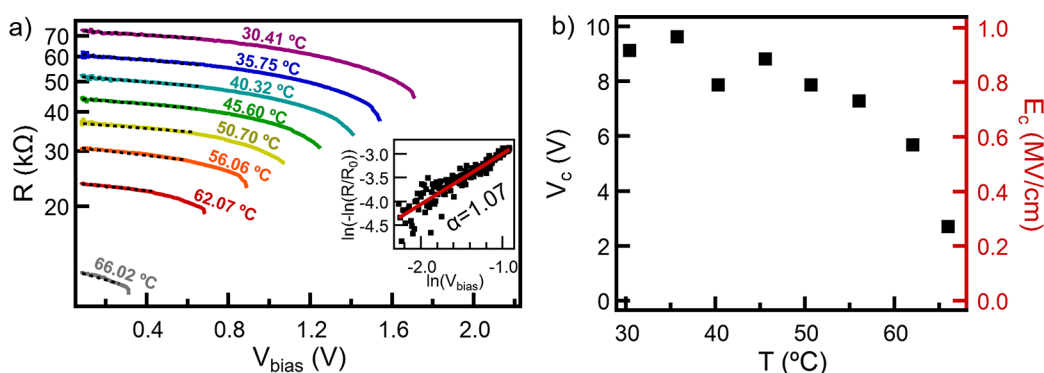


Figure 3. Influence of electric field on the device operation. a) $R(V)$ traces measured at different temperatures. All traces show the similar nonlinear current behavior at low bias voltage (see dashed lines). The inset shows the $\ln(-\ln(R/R_0))$ vs $\ln(V)$ relation at 56.06 °C base temperature whose slope determines the α exponent, introduced in eq 1) Temperature dependence of characteristic voltage (V_c) by fitting the low voltage part of each $R(V)$ trace. According to the finite element simulations the characteristic voltage converts to a characteristic electric field with a constant scaling factor, $E_c = V_c/99.5$ nm, as shown on the right axis.

maximum value. The set voltages show a very clear decreasing tendency as the temperature increases, however, this trend can be qualitatively described by both the thermally and electrically triggered MIT. For more detailed analysis we captured statistical ensemble of switching cycles to study the set voltage (V_{set}), the set current (I_{set}) and the set power (P_{set}) as a function of the base temperature, see Figure 2b–d. Each point, except the highest temperature, is the average of 10 consecutive switching cycles induced by identical triangular voltage signals at the same temperature. The highest base temperature was very close to T_c (being inside the hysteresis loop of the $R(T)$ curve in Figure 1e), thereby the device was stuck in the metallic state for the majority of switching cycles, that is, at this temperature only the switching parameters of the first (positive polarity) switching cycle are presented. The standard deviations of the averaged values are smaller than the size of the dots. The black/blue dots show the switching parameters extracted from the positive/negative voltage polarity. The slightly lower values at negative polarity are the consequence of Thomson-effect.^{32,33} The V_{set} , except the highest temperature, shows linearly decreasing tendency, which is highlighted by a guide to the eye line (see red line in Figure 2b), whereas I_{set} has roughly constant value of around 40 μ A (Figure 2c). Accordingly, the switching power ($P_{set} = V_{set} \cdot I_{set}$) shows nearly the same tendency as the set voltage.

After the above electrical analysis, another $R(T)$ trace was measured to verify the device stability. Figure 2e shows that there is no substantial difference between the initial (black curve) and the final (blue) hysteresis curve, only the phase transition became more abrupt. This finding implies that the metal electrodes and the VO_2 layer did not exhibit any significant modification during the electrical operation. Moreover, the two temperature sweeps match extremely well in the semiconducting state, which enables us to use the low voltage temperature dependent resistance of the device as a reliable thermometer,³⁴ that is, we can determine the local temperature very precisely from the resistance measured at low enough bias.

From the measured $I(V)$ curves (Figure 2a) the voltage dependent resistance, $R(V) = V/I$ can be plotted (Figure 3a) at various base temperatures, which will be a key object of our further analysis, solely focusing on the $R(V)$ curves of the HRS up to the onset of the set transition. The $R(V)$ curves of the LRS would exhibit a basically Ohmic behavior with much

smaller nonlinearity due to the metallic nature of the LRS (see the LRS branches in Figure 1f).

First, we consider the two extreme cases, when only either the thermal^{35–38} or electrical effect^{39–42} is responsible for the MIT. In case of a pure thermally induced transition and assuming temperature independent thermal transport parameters, P_{set} is expected to scale linearly with the temperature decreasing to zero at T_c .⁴³ In our case, although the power data also follow a linear tendency (see red guide to the eye line in Figure 2d), the extrapolation of the points does not cut the temperature axis at the transition temperature, $T_c = 66.22$ °C, instead at a significantly higher temperature (≈ 80 °C). This finding indicates that the thermal effect probably plays an important role in the MIT, but either strongly temperature dependent thermal transport parameters are concerned, or nonlinear conduction phenomena are also crucial in the switching process. Furthermore, a solely Joule heating-based model would yield zero slope for the $R(V)$ curve around zero bias, since in this region the dissipated power is negligible due to the $P \sim V^2$ relation. This also contradicts the experimental observations with a significant decrease of the resistance in the low bias region (see the dashed lines in Figure 3a).

In the other extreme case, the pure electric field triggered phase transition would also yield the decrease of V_{set} with increasing base temperature, since the breakdown electric field decreases with the temperature. However, the switching power is not expected to follow the observed linearly decreasing trend.^{39–41} Nevertheless, the electric field must have a significant influence on our device's operation, since in our nanogap arrangement small bias voltage leads to high electric field and prior the switching event the field can reach the extremely high values exceeding 0.5 MV/cm, which can solely be enough to induce the phase transition in some devices.⁴⁰

Next, we gain further insight into the possible nonlinear conduction phenomena by a more detailed analysis of the $R(V)$ curves. The high electric-field induced carrier generation can indeed produce a finite slope of the $R(V)$ curve around zero bias, which was already reported in the literature.^{23,44,45} Several conduction mechanisms were applied to describe the nonlinear $I(V)$ behavior of VO_2 layers, which all can be summarized in the following form:

$$R(V_{bias}, T) \approx R_0(T) \cdot \exp[-(V_{bias}/V_c)^\alpha] \quad (1)$$

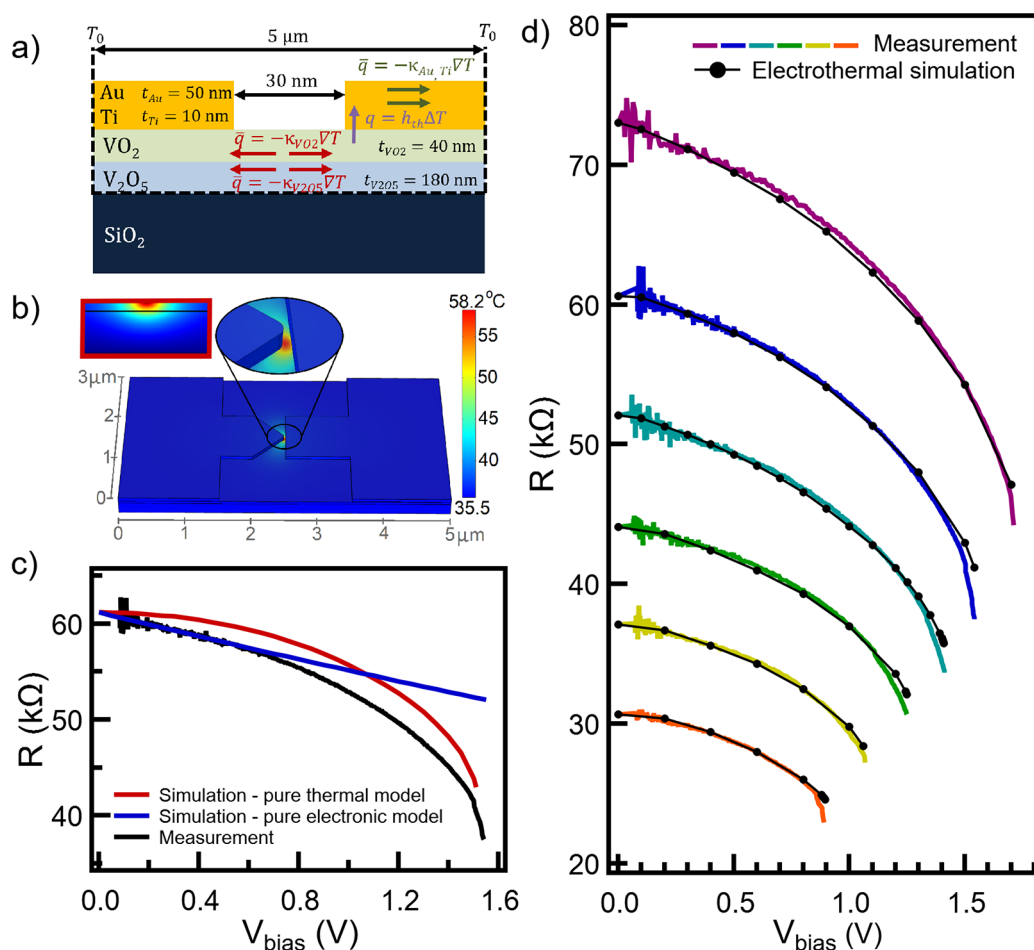


Figure 4. Finite element simulation of the nanogap device. a) Schematic of the thermal model of the device, introducing the most relevant geometry parameters and the heat transfer mechanisms with the corresponding heat equations. The values of the thermal parameters are presented in the Methods. b) The simulated temperature profile with $V_{\text{bias}} = 1.5$ V and $T_0 = 35.75$ °C, showing the realistic device geometry. The magnified view of the gap shows the focused ultrasmall active region. The inset with the red frame demonstrates the cross-sectional temperature profile in the middle of the active region, where the black line represents the boundary between the VO₂ and V₂O₅ layers. c) Results of pure thermal and pure electronic simulation. The thermal model (red curve) cannot reproduce the initial decreasing tendency of the $R(V)$ curve due to the negligible Joule heating. The pure electronic model (blue curve) has a constant nonlinearity due to the lack of Joule heating and diverges from the measured $R(V)$ curve (black) at higher bias. d) Measured (colored curves) and simulated $R(V)$ characteristics (black curves) using the combined electronic and thermal model. The simulated traces show very good agreement with the measurement at each base temperature between 30.41 and 56.06 °C.

where $R_0(T)$ is the temperature dependent low voltage resistance shown in Figure 2e, V_{bias} is the voltage drop on the device, and V_c is a characteristic voltage, whereas the α exponent specifies the conduction mechanism. As possible conduction mechanisms, the Poole-Frenkel conduction^{45–49} can be described by $\alpha = 0.5$, the phonon assisted tunneling^{23,50} gives $\alpha = 2$ or the Zener tunneling^{51–53} yields $\alpha = 1$.

The dominant conduction mechanism of our device was determined by fitting the $\ln(-\ln(R/R_0))$ vs $\ln(V_{\text{bias}})$ curves to a line in the $V_{\text{bias}} = 0.05$ – 0.4 voltage region (see inset of Figure 3b), whose slope serves the α parameter. The exponents were close to unity (varied between 0.9–1.07) at all temperatures referring to Zener conduction. This finding is confirmed by measurements on further devices with similar or significantly larger electrode separation (see Figure 6 in the Methods). Next, we determined the characteristic voltage (V_c) in the Zener conduction model (that is, fixing $\alpha = 1$) by fitting the low voltage part of $\ln(R) - V_{\text{bias}}$ graph to a line (see dashed lines in Figure 3a). The fitted V_c values are presented in Figure 3b (black squares) exhibiting a moderate variation with the external temperature further away from T_c and a significant

decrease close to the phase transition temperature. Note, however, that the data points above 60 °C are already inside the hysteresis loop of the phase transition (see Figure 2e), where the coexistence of the two phases is conceivable.

Our analysis so far demonstrates that a purely Joule heating-based model fails to describe some important features in the measurements, most importantly the offset of the P_{set} vs T relation from the envisioned zero switching power at T_c and the nonzero zero-bias slopes of the $R(V)$ curves. To better understand the contribution of nonlinear electronic phenomena to these features, we performed steady-state finite element simulations in COMSOL Multiphysics implementing the exact geometry of the device (see the SEM image in Figure 1b and the model geometry in Figure 4b). The layer structure of the model with the most relevant dimensions is schematically presented in Figure 4a, mimicking the result of the TEM and EELS measurements. Figure 4a also shows the considered heat conduction mechanisms (marked by colored arrows) and thermal boundary conditions (marked by dashed black line). Besides the bulk heat conduction of the VO₂ and V₂O₅ layers and the metal electrodes (red and green arrows), we

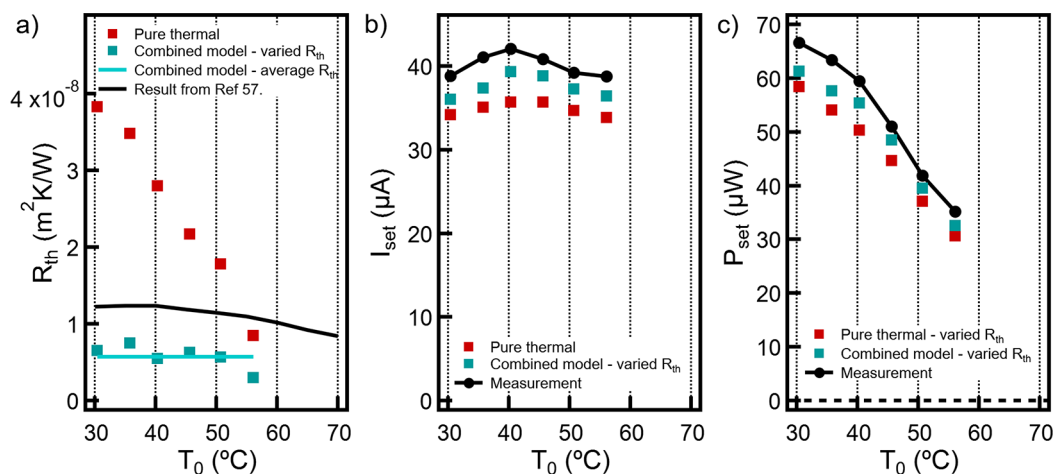


Figure 5. Scaling of the thermal and switching parameters with the base temperature. a) The thermal boundary resistance (R_{th}) as a function of the base temperature under different simulational conditions. The red squares represent the results of pure thermal simulation, whereas the turquoise squares are obtained by the combined electronic and thermal model. The black trendline illustrates the experimentally measured value of R_{th} between VO_2 and Ti obtained in ref 57. b) The measured (black circles with line) and simulated (colored squares) I_{set} versus T_0 . Both the pure thermal model (red squares) combined electronic and thermal model (turquoise squares) reproduce the nearly constant tendency, however, the latter model gives significantly better estimation and shows similar fluctuation as the measured data. c) The measured P_{set} (black circles with line) is also well fitted by the combined electronic and thermal simulation (turquoise squares), whereas the pure thermal simulation (red squares) more strongly underestimates the switching power.

considered a thermal boundary conductance at the VO_2/Ti interface^{54–56} (h_{th} , purple arrow). The latter is considered as a fitting parameter in our model, whereas the rest of the thermal characteristics are taken from literature values (see Methods for the details). The boundary condition presumes that the edge of the simulated part of the device and the bottom surface of the V_2O_5 layer are thermally anchored to the ambient (T_0), as indicated by the black dashed lines. The three-dimensional picture of the simulated realistic contact geometry together with the color-scaled demonstration of the simulated self-heating in the active region is demonstrated in Figure 4b.

In our detailed finite element analysis, the spatial variation of both the local temperature ($T(r)$) and the local electric field ($E(r)$) are determined, and the local resistivity is calculated as

$$\rho(E, T) = \rho_0(T) \cdot \exp[-(E/E_c)^\alpha] \quad (2)$$

Note that at low bias the self-heating is negligible and therefore the $\rho_0(T)$ resistivity converts from $R_0(T)$ by a simple geometrical scaling factor, which is determined by a constant temperature finite element simulation according to the realistic device geometry. This conversion is also demonstrated by the scaling of the resistance (left axis) to resistivity (right axis) in Figure 2e. The deduction of E_c from the above-defined characteristic voltage, V_c is less straightforward, but $E_c \approx V_c/d$ is considered as a reasonable order-of-magnitude approximation, where $d \approx 30$ nm is the distance of the two electrodes. This first approximation is refined by the finite element simulation, where E_c is also considered as an adjustable parameter. As a simplification, in the simulation a constant (temperature independent) characteristic electric field (E_c) was applied.

To demonstrate that neglecting either the thermal or the electronic phenomena leads to insufficient description, we plotted a measured $R(V)$ trace at 35.75 °C (black curve) with its best fittings with either a purely thermal or purely electronic model, (Figure 4c). The red trace shows the result when the field dependence was eliminated from the model (that is, $\rho(E, T) = \rho_0(T)$) and the resistance changes solely due to the self-

heating effect. In this case, the thermal boundary conductance, h_{th} is adjusted such, that the experimentally measured set voltage coincides with the simulated voltage, where the transition temperature is first reached in the junction. Without the nonlinear electronic contribution the resistance has a nearly constant value at low bias due to the negligible Joule heating and the nonlinearity appears only at higher bias, that is, the simulated $R(V)$ trace significantly differs from the measured one. Similarly, we simulated the field dependent resistance, assuming no self-heating effect (blue curve). In this case, the E_c value estimated from the $\ln(R)$ vs V_{bias} traces is further fine-tuned to obtain a perfect match between the finite low-bias slopes of the measured and simulated $R(V)$ traces. This limiting case fails to describe the nonlinearity of the $R(V)$ trace yielding a significant deviation from the measured data in the high bias region. Accordingly, we can conclude that neither the pure thermal model nor the pure electronic model is suitable to describe the fine details of the device characteristics.

In contrast, Figure 4d shows the results of the combined electronic and thermal simulation at different base temperatures (black circles with line) using the temperature and electric field dependent resistivity (eq 2). The measured $R(V)$ curves (colored curves) are well fitted by the simulation, all of them fulfill both criteria, namely, they have correct slope at low bias and follow the same high bias nonlinearity due to the self-heating. Considerable deviations can be observed only right before the switching events, which may be caused by the temperature dependence of E_c . Close to the switching voltage, E_c presumably reduces locally at the higher temperature part of the active region, which was, however, not included in the simulation. With this simplification, our model relies on two adjustable parameters, the thermal boundary resistance ($R_{th} = 1/h_{th}$), whose value was set to obtain the same set voltage as in the measurement, and E_c , whose value is first roughly estimated from the slope of the $\ln(R)$ vs V_{bias} data, and then it is fine-tuned to perfectly reproduce the finite low-bias slope of the $R(V)$ curve. We found that the best suited E_c values at all base temperatures can be determined by rescaling V_c by the

same $d_{\text{eff}} = 99.5$ nm effective gap size (see the right axis in Figure 3b), which is three times larger than the actual electrode distance. This deviation is attributed to the highly inhomogeneous electric field profile in the gap region. Around the tip of the triangular-shaped electrode, the electric field can approach the value of E_c when V_{set} is applied, however, in the midgap region and away from the electrodes it decreases substantially, lowering the average electric field.

Finally, we compare the results of the pure thermal simulation and the combined electronic and thermal simulation on the level of the switching parameters (I_{set} and P_{set} ; see Figures 5b,c) and the extracted thermal boundary resistance, R_{th} (Figure 5a). In the former two panels, the measured data are shown by black circles, whereas the results of the pure thermal/electrothermal simulation are represented by the red/turquoise squares. Both models reproduce the trends of the measured I_{set} and P_{set} data, but the combined electronic and thermal model provides a seemingly better agreement also mimicking the fluctuation pattern of the measured data. Note, however, that the slightly lower values of I_{set} and P_{set} stem from the substantially increased nonlinearity right before the switching event in the experimental data (Figure 4d). We believe that the steep increase of the current results from the stronger temperature dependence of the thermal and electrical parameters of the VO_2 layer close to the phase transition, as well as fluctuation phenomena in the temperature range, where the two phases may coexist (see the hysteretic phase transition in Figure 1e). These phenomena arising in the close proximity of the phase transition cannot be implemented reliably in our model, therefore the simulation serves somewhat lower set parameters.

The extracted R_{th} values (Figure 5a), however, show a remarkable difference between the two models. The pure thermal model (red squares) exhibits a very strong temperature dependence of R_{th} , which seems to be incompatible with the previous experimental observations,^{57,58} as demonstrated by the black trendline in Figure 5 illustrating the measured R_{th} vs T_0 curve of a Ti/VO_2 interface published in ref 57. The results of the combined electronic and thermal model, however, yield R_{th} values with a much weaker temperature dependence (turquoise squares in Figure 5a). The latter is also consistent with the results of ref 57, even though the magnitude of R_{th} is expected to be sensitive to the details of the sample preparation. This analysis again underpins the importance of the combined electronic and thermal model in the description of the temperature and voltage dependent characteristics of VO_2 resistive switches. It is also noted, that the combined electronic and thermal model yields a more-or-less temperature independent thermal boundary resistance (see the turquoise line representing the average R_{th} in Figure 5c), and E_c also shows a modest variation below the hysteresis loop of the phase transition (<60 °C, see Figure 2e), that is, a sufficiently good description is already obtained by using a fixed (temperature independent) E_c and R_{th} parameters in the model.

3. CONCLUSIONS

In conclusion, we developed VO_2 resistive switching junctions with a focused, nanosized active region. Our electrode-separation-dependent measurements demonstrated the clear decrease of the set voltage with decreasing gap size, which underpins the advantage of the demonstrated confined device geometry with respect to energy consumption. Furthermore,

our novel device geometry confines the active region to a rather well-defined spatial spot instead of more complex, percolation-like spatial patterns.^{20–23} The analysis of the voltage and temperature dependent conduction properties of these devices has pointed out the interplay of local Joule heating and nonlinear transport features in the local insulator-to-metal transition, also indicating a Zener tunneling type conduction mechanism in the high resistance state. Furthermore, the simplified, focused device geometry facilitated the finite element simulation of the device operation. These simulations also underpinned the failure of a purely thermal or purely electronic model, but demonstrated a precise agreement with the experimental observations for the combined electronic and thermal simulation. This analysis provides a detailed insight into the local temperature and electric field profiles in the single-spot active region, as well as into the relevant parameters describing the thermal transport and the nonlinear conduction mechanisms, facilitating the understanding as well as the thermal and electronic design of novel VO_2 -based neuronal devices.

4. METHODS

4.1. Preparation and Characterization of VO_2 Thin Film. The 100 ± 4 nm thick metallic vanadium thin film was deposited on (100)-oriented Si wafers covered by $1 \mu\text{m}$ SiO_2 . Post deposition heat treatment was carried out in a tube furnace at 400 °C for 4.5 h under 0.1 mbar sparse air to oxidize the metallic film.²⁵ For cross-sectional compositional analysis TEM lamellas were cut from the sample. This analysis yielded two different regions separated by a well-defined boundary (dark and light gray regions in Figure 1d inset). Note that the darkest top gray layer is a platinum cover film, which serves as a protective layer during the TEM specimen preparation. The TEM analysis yielded the polycrystalline structure of the bottom layer with lateral grain size on the order of 200 nm. EELS spectra were measured on these two layers (blue and red spectra at the blue and red dot positions in Figure 1d), and were compared to calibration measurements on standard V_2O_5 , VO_2 , and V_2O_3 samples. The latter respectively yielded L3 peak positions of 517.5 , 516.8 , and 515.4 eV for these three oxidation states. The EELS spectra on our devices yield L3 peak positions at 517.4 and 516.9 eV for the blue and red spectra, which are close to the V_2O_5 and VO_2 calibration values. Another characteristic feature of the calibration measurements yielded the composition dependence of the L3/L2 intensity ratio. This precisely coincides with the V_2O_5 calibration measurement for the blue spectrum in our sample, but for the red spectrum the anticipated VO_2 composition should yield smaller L2 intensity. On the basis of these results, the blue EELS spectrum is consistent with the V_2O_5 composition, whereas the slight decrease of the L3 peak position for the red spectrum is indicative of the VO_2 composition. Whereas the latter is a less definite statement according to the spectrum, the presence of VO_2 in the top layer is quite clear from the electrical characterization measurements (Figure 1d,e).

4.2. Sample Preparation and Characterization. The metal electrodes were patterned by electron-beam lithography, followed by electron-beam evaporation of 50 nm thick Au with a 10 nm thick Ti adhesion layer. For our ultrasmall devices the nominal gap size between the two electrodes was kept constant (30 nm) in the design, while the exposure dose of the 300 nm thick PMMA resist during electron beam lithography process was varied in the range of 220 – $260 \mu\text{C}/\text{cm}^2$ which resulted in different electrode separation (d). As a comparison, we have also performed measurements on devices with intentionally increased gap sizes. After the sample preparation, SEM images were taken of the as-prepared samples to determine the gap size between the metal electrodes. The room temperature electrical characterization was performed on several devices, and stable electrical switching could be induced in all cases. Figure 6a shows the set voltage (V_{set}) statistics of samples with varied gap sizes, for

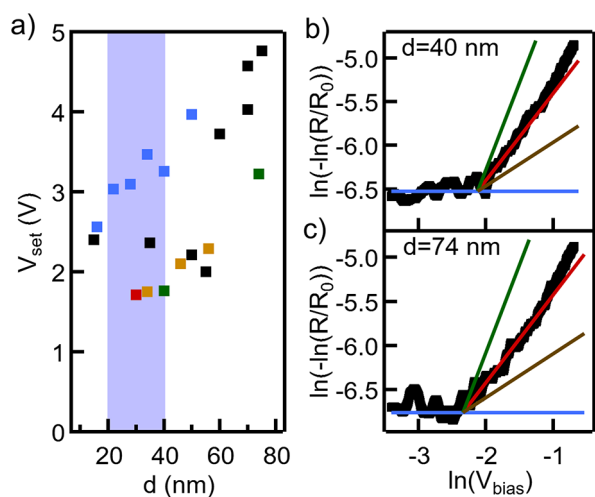


Figure 6. Influence of the electrode separation on the electrical characteristics of VO₂ devices. a) V_{set} versus electrode separation (d) shows an increasing set voltage trend with the gap size. Different colors correspond to different VO₂ substrates. The red dot marks the device used for the simulation in the main text. b,c) $I(V)$ traces of two samples with different active region sizes on $\ln(-\ln(R/R_0))$ vs $\ln(V)$ graph. At low voltage, the devices show linear $I(V)$ characteristics ($\alpha = 0$), which change to Zener tunneling ($\alpha = 1$) at higher bias voltage. The green, red, brown, and blue lines respectively indicate α values of 2, 1, 0.5, and 0.

which the same color marks the devices prepared on the same VO₂ layer. Each point corresponds to the average of 50 consecutive switching cycles. The same tendency was observed for all substrates, the set voltage increases with the electrode separation. However, among the different substrates the switching voltages show larger variability. The detailed study, presented in the main text, was performed on the sample marked by the red dot. To identify the relevant transport mechanism in case of the different device geometries, we determined the α exponent for various samples. Figure 6b,c shows the proper plot of $I(V)$ characteristic of two devices with different gap sizes (green dots in Figure 6a). We have found that at low bias voltage (<100 mV) α has nearly zero value, which can refer to Ohmic conduction, whereas at the higher bias voltage its value changes to unity (see the red lines with unity slope). At even higher bias voltage (>400 mV) the measurement data deviate from a line due to the increased Joule heating. As a comparison, the green, brown, and blue lines respectively represent $\alpha = 2$ (Poole-Frenkel conduction), $\alpha = 0.5$ (phonon assisted tunneling), and $\alpha = 0$ (Ohmic conduction). It is clear that all these trendlines strongly deviate from the data, implying that indeed Zener tunneling is the typical conduction mechanism in our VO₂ devices, regardless of the gap size in the 15–75 nm regime. We note, however, that the steepness of the nonlinearity and the related relevant transport mechanism are found to be sensitive to preparation method and the material aspects of the VO₂ layer,²³ that is, our results indicating Zener tunneling mechanism could not be generalized for samples with similar design, but different layer preparation method.

4.3. Transport Measurements. To perform electrical transport measurements the Si substrate was fixed to a printed circuit board (PCB) and the devices were bonded to copper plates on the PCB. The base temperature was controlled by a Peltier module fixed to the back side of the PCB, whereas temperature near the devices was recorded by a Pt-1000 sensor during the $R(T)$ measurement (see Figure 2e). Afterward these $R(T)$ traces served as a calibration curve to determine the base temperature value precisely during the detailed device characterization process (see Figure 2a–d). During the acquisition of the current–voltage ($I(V)$) characteristics, the VO₂ device and the serial resistor (R_s) were driven by a data acquisition card by applying low frequency triangular voltage output signal

(V_{drive}). The device's current was monitored by a current amplifier while the V_{bias} voltage drop on the junction was determined numerically as $V_{\text{bias}} = V_{\text{drive}} - I \cdot R_s$.

4.4. Finite Element Simulation. We examined electrothermal heating in the device by finite-element method simulations implemented through COMSOL Multiphysics software. The combined electronic and thermal model couples electrodynamics and heat transfer physics. The dimensions of the simulated $3 \times 5 \times 0.28 \mu\text{m}^3$ large part of the device are identical to those of the real one (see Figure 4b) and the radius of curvature of the triangular electrode is set to 50 nm. The modeling assumes that all surfaces and interfaces are perfectly flat and that the materials are microscopically homogeneous and isotropic. The thermal parameters of the vanadium-oxides were taken from literature values. The thermal conductivity of the VO₂ was given by step function, considering that it changes during the phase transition: $\kappa_{\text{VO}_2} = 3.5$ W/mK if $T < T_c$ and $\kappa_{\text{VO}_2} = 6$ W/mK if $T > T_c$.^{55,59} The thermal conductivity of V₂O₅ varies in wide range in the literature, between 0.45 and 3.84 W/mK, according to the crystalline structure and measurement methods.^{60,61} We used an intermediate value of $\kappa_{\text{V}_2\text{O}_5} = 1.75$ W/mK, which was measured on crystalline, 150 nm thick film.⁶² For the metal electrodes we used the built-in values of $\kappa_{\text{Au}} = 311$ W/mK and $\kappa_{\text{Ti}} = 21.9$ W/mK for the thermal conductivity and $\sigma_{\text{Au}} = 45.6 \cdot 10^6$ S/m and $\sigma_{\text{Ti}} = 2.6 \cdot 10^6$ S/m for the electrical conductivity. In case of the V₂O₅ layer, $\sigma_{\text{V}_2\text{O}_5} = 0.04$ S/m value was taken from the literature,⁶³ whereas the electrical conductivity of the VO₂ layer was deduced from the experimental R – T curve (see Figure 2e). The COMSOL simulations were performed with 2, 3, 5, and 10 nm grid size in the active region, yielding less than 0.5% difference in the simulated current and temperature values. Relying on this, the 5 nm grid size was generally applied in the simulation as an optimal compromise between speed and accuracy. To check the importance of the boundary conditions, in particular the bottom SiO₂ layer in the thermal transport, we have performed a reference simulation in the opposite extreme limit, where the SiO₂ layer was completely removed, that is, the heat could only flow toward the sides, but the bottom of the V₂O₅ sublayer was isolated from the environment. This drastic change in the boundary condition yielded a relatively small ($\approx 7\%$) increase of maximum temperature increment ($\Delta T = T_{\text{max}} - T_0$) in the active region, by applying a voltage close to V_{set} . The relative change in the electrical current was even smaller ($\approx 4\%$). Our realistic device geometry is between these two extremities (perfect/no heat conduction at the SiO₂ interface), that is, we would only expect minor changes of the simulated results compared to the simplified boundary condition in our work. Furthermore, as R_{th} is a fitting parameter in our work, a minor change in the bottom boundary condition is easily compensated by a minor change in R_{th} leaving the $R(V)$ characteristics practically unchanged.

■ ASSOCIATED CONTENT

Data Availability Statement

The data sets generated and/or analyzed during the current study are available from the corresponding author (L.P.) on reasonable request.

■ AUTHOR INFORMATION

Corresponding Author

László Pósa – Institute of Technical Physics and Materials Science, Centre for Energy Research, 1121 Budapest, Hungary; Department of Physics, Institute of Physics, Budapest University of Technology and Economics, H-1111 Budapest, Hungary; orcid.org/0000-0001-7303-4031; Email: posa.laszlo@ek-cer.hu

Authors

Péter Hornung – Institute of Technical Physics and Materials Science, Centre for Energy Research, 1121 Budapest, Hungary

Timea Nóra Török – Institute of Technical Physics and Materials Science, Centre for Energy Research, 1121 Budapest, Hungary; Department of Physics, Institute of Physics, Budapest University of Technology and Economics, H-1111 Budapest, Hungary; orcid.org/0000-0001-5238-5895

Sebastian Werner Schmid – Department of Physics, Institute of Physics, Budapest University of Technology and Economics, H-1111 Budapest, Hungary; orcid.org/0000-0003-4866-6859

Sadaf Arjmandabasi – Department of Physics, Institute of Physics, Budapest University of Technology and Economics, H-1111 Budapest, Hungary

György Molnár – Institute of Technical Physics and Materials Science, Centre for Energy Research, 1121 Budapest, Hungary; orcid.org/0000-0002-4792-5516

Zsófia Baji – Institute of Technical Physics and Materials Science, Centre for Energy Research, 1121 Budapest, Hungary

Goran Dražić – Department of Materials Chemistry, National Institute of Chemistry, SI-1000 Ljubljana, Slovenia; orcid.org/0000-0001-7809-8050

András Halbritter – Department of Physics, Institute of Physics, Budapest University of Technology and Economics, H-1111 Budapest, Hungary; ELKH-BME Condensed Matter Research Group, Budapest University of Technology and Economics, H-1111 Budapest, Hungary

János Volk – Institute of Technical Physics and Materials Science, Centre for Energy Research, 1121 Budapest, Hungary

Complete contact information is available at:
<https://pubs.acs.org/10.1021/acsanm.3c00150>

Author Contributions

The nanogap devices were developed and prepared by L.P. The electrical transport measurements were performed by L.P., T.N.T., and S.A. The electrical characterization of samples with variable gap sizes was performed by S.W.S. and T.N.T. The finite element simulation was performed by P.H. The data analysis of the measured and the simulated data was performed by L.P., P.H., A.H., and J.V. The VO₂ layer was produced by Gy.M. The EELS and TEM were performed by G.D. The data analysis of EELS and TEM data was performed by Zs.B. and G.D. The manuscript was written by L.P. and A.H. The project was supervised by L.P., A.H., and J.V. All authors contributed to the discussion of the results.

Notes

The authors declare no competing financial interest.

ACKNOWLEDGMENTS

This research was supported by the Ministry of Culture and Innovation and the National Research, Development and Innovation Office within the Quantum Information National Laboratory of Hungary (Grant No. 2022-2.1.1-NL-2022-00004) and the NKFI K128534, K143169 and K143282 grants. L.P. acknowledges the support of the UNKP-21-4 new national excellence program of the Ministry for Innovation and Technology from the source of the National Research, Development and Innovation Fund and János Bolyai Research Scholarship. Project no. 963575 has been implemented with the support provided by the Ministry of Culture and Innovation of Hungary from the National Research, Development, and Innovation Fund, financed under the KDP-2020 funding scheme.

REFERENCES

- (1) Manca, N.; Kanki, T.; Endo, F.; Marré, D.; Pellegrino, L. Planar Nanoactuators Based on VO₂ Phase Transition. *Nano Lett.* **2020**, *20*, 7251–7256.
- (2) Wang, T.; Torres, D.; Fernández, F. E.; Wang, C.; Sepúlveda, N. Maximizing the performance of photothermal actuators by combining smart materials with supplementary advantages. *Sci. Advances* **2017**, *3*, No. e1602697.
- (3) Li, G.; Xie, D.; Zhong, H.; Zhang, Z.; Fu, X.; Zhou, Q.; Li, Q.; Ni, H.; Wang, J.; Guo, E.-j.; He, M.; Wang, C.; Yang, G.; Jin, K.; Ge, C. Photo-induced non-volatile VO₂ phase transition for neuromorphic ultraviolet sensors. *Nat. Commun.* **2022**, *13*, 1729.
- (4) Strelcov, E.; Lilach, Y.; Kolmakov, A. Gas Sensor Based on Metal Insulator Transition in VO₂ Nanowire Thermistor. *Nano Lett.* **2009**, *9*, 2322–2326.
- (5) Hu, B.; Ding, Y.; Chen, W.; Kulkarni, D.; Shen, Y.; Tsukruk, V. V.; Wang, Z. L. External-Strain Induced Insulating Phase Transition in VO₂ Nanobeam and Its Application as Flexible Strain Sensor. *Adv. Mater.* **2010**, *22*, 5134–5139.
- (6) Zhou, Y.; Ramanathan, S. Correlated Electron Materials and Field Effect Transistors for Logic: A Review. *Critical Reviews in Solid State and Materials Sciences* **2013**, *38*, 286–317.
- (7) Shukla, N.; Thathachary, A. V.; Agrawal, A.; Paik, H.; Aziz, A.; Schlom, D. G.; Gupta, S. K.; Engel-Herbert, R.; Datta, S. A steep-slope transistor based on abrupt electronic phase transition. *Nat. Commun.* **2015**, *6*, 7812.
- (8) Yajima, T.; Nishimura, T.; Toriumi, A. Positive-bias gate-controlled metal–insulator transition in ultrathin VO₂ channels with TiO₂ gate dielectrics. *Nat. Commun.* **2015**, *6*, 10104.
- (9) Yi, W.; Tsang, K. K.; Lam, S. K.; Bai, X.; Crowell, J. A.; Flores, E. A. Biological plausibility and stochasticity in scalable VO₂ active memristor neurons. *Nat. Commun.* **2018**, *9*, 4661.
- (10) del Valle, J.; Salev, P.; Tesler, F.; Vargas, N. M.; Kalchauer, Y.; Wang, P.; Trastoy, J.; Lee, M.-H.; Kassabian, G.; Ramirez, J. G.; Rozenberg, M. J.; Schuller, I. K. Subthreshold firing in Mott nanodevices. *Nature* **2019**, *569*, 388–392.
- (11) Wu, Q.; Dang, B.; Lu, C.; Xu, G.; Yang, G.; Wang, J.; Chuai, X.; Lu, N.; Geng, D.; Wang, H.; Li, L. Spike Encoding with Optic Sensory Neurons Enable a Pulse Coupled Neural Network for Ultraviolet Image Segmentation. *Nano Lett.* **2020**, *20*, 8015–8023.
- (12) Corti, E.; Cornejo Jimenez, J. A.; Niang, K. M.; Robertson, J.; Moselund, K. E.; Gotsmann, B.; Ionescu, A. M.; Karg, S. Coupled VO₂ Oscillators Circuit as Analog First Layer Filter in Convolutional Neural Networks. *Front. Neurosci.* **2021**, *15*, 628254.
- (13) Corti, E.; Gotsmann, B.; Moselund, K.; Ionescu, A. M.; Robertson, J.; Karg, S. Scaled resistively-coupled VO₂ oscillators for neuromorphic computing. *Solid-State Electron.* **2020**, *168*, 107729.
- (14) Bohachuk, S. M.; Kumar, S.; Pitner, G.; McClellan, C. J.; Jeong, J.; Samant, M. G.; Wong, H.-S. P.; Parkin, S. S. P.; Williams, R. S.; Pop, E. Fast Spiking of a Mott VO₂–Carbon Nanotube Composite Device. *Nano Lett.* **2019**, *19*, 6751–6755.
- (15) Rocco, R.; del Valle, J.; Navarro, H.; Salev, P.; Schuller, I. K.; Rozenberg, M. Exponential Escape Rate of Filamentary Incubation in Mott Spiking Neurons. *Phys. Rev. Appl.* **2022**, *17*, 024028.
- (16) Cheng, S.; Lee, M.-H.; Tran, R.; Shi, Y.; Li, X.; Navarro, H.; Adda, C.; Meng, Q.; Chen, L.-Q.; Dynes, R. C.; Ong, S. P.; Schuller, I. K.; Zhu, Y. Inherent stochasticity during insulator-metal transition in VO₂. *Proc. Natl. Acad. Sci. U. S. A.* **2021**, *118*, No. e2105895118.
- (17) Zhou, X.; Gu, D.; Li, Y.; Qin, H.; Jiang, Y.; Xu, J. A high performance electroformed single-crystallite VO₂ threshold switch. *Nanoscale* **2019**, *11*, 22070–22078.
- (18) Yuan, R.; Duan, Q.; Tiw, P. J.; Li, G.; Xiao, Z.; Jing, Z.; Yang, K.; Liu, C.; Ge, C.; Huang, R.; Yang, Y. A calibratable sensory neuron based on epitaxial VO₂ for spike-based neuromorphic multisensory system. *Nat. Commun.* **2022**, *13*, 3973.
- (19) Samizadeh Nikoo, M.; Soleimanzadeh, R.; Krammer, A.; Migliato Marega, G.; Park, Y.; Son, J.; Schueler, A.; Kis, A.; Moll, P. J. W.; Matoli, E. Electrical control of glass-like dynamics in vanadium

dioxide for data storage and processing. *Nature Electronics* **2022**, *5*, 596–603.

(20) del Valle, J.; Vargas, N. M.; Rocco, R.; Salev, P.; Kalcheim, Y.; Lapa, P. N.; Adda, C.; Lee, M.-H.; Wang, P. Y.; Fratino, L.; Rozenberg, M. J.; Schuller, I. K. Spatiotemporal characterization of the field-induced insulator-to-metal transition. *Science* **2021**, *373*, 907–911.

(21) del Valle, J.; Rocco, R.; Domínguez, C.; Fowlie, J.; Gariglio, S.; Rozenberg, M. J.; Triscone, J.-M. Dynamics of the electrically induced insulator-to-metal transition in rare-earth nickelates. *Phys. Rev. B* **2021**, *104*, 165141.

(22) Gu, M. J.; Lin, S.; Xu, X. F.; Wang, C. R.; Wu, B. H.; Cao, J. C. Random-resistor network modeling of resistance hysteresis of vanadium dioxide thin films. *J. Appl. Phys.* **2022**, *132*, 015301.

(23) Kalcheim, Y.; Camjayi, A.; del Valle, J.; Salev, P.; Rozenberg, M.; Schuller, I. K. Non-thermal resistive switching in Mott insulator nanowires. *Nat. Commun.* **2020**, *11*, 2985.

(24) Gubicza, A.; Manrique, D. Z.; Pósa, L.; Lambert, C. J.; Mihály, G.; Csontos, M.; Halbritter, A. Asymmetry-induced resistive switching in Ag-Ag₂S-Ag memristors enabling a simplified atomic-scale memory design. *Sci. Rep.* **2016**, *6*, 30775.

(25) Pósa, L.; Molnár, G.; Kalas, B.; Baji, Z.; Czirány, Z.; Petrik, P.; Volk, J. A Rational Fabrication Method for Low Switching-Temperature VO₂. *Nanomaterials* **2021**, *11*, 212.

(26) Kalavathi, S.; Amirthapandian, S.; Chandra, S.; Sahu, P. C.; Sahu, H. K. Valence state, hybridization and electronic band structure in the charge ordered AlV₂O₄. *J. Phys.: Condens. Matter* **2014**, *26*, 015601.

(27) Moatti, A.; Sachan, R.; Prater, J.; Narayan, J. Control of Structural and Electrical Transitions of VO₂ Thin Films. *ACS Appl. Mater. Interfaces* **2017**, *9*, 24298–24307.

(28) Moatti, A.; Sachan, R.; Gupta, S.; Narayan, J. Vacancy-Driven Robust Metallicity of Structurally Pinned Monoclinic Epitaxial VO₂ Thin Films. *ACS Appl. Mater. Interfaces* **2019**, *11*, 3547–3554.

(29) Zhang, Z.; Chen, J.; Guo, Y.; Robertson, J. Band alignment calculation of dielectric films on VO₂. *Microelectron. Eng.* **2019**, *216*, 111057.

(30) Lu, H.; Clark, S.; Guo, Y.; Robertson, J. Modelling the enthalpy change and transition temperature dependence of the metal–insulator transition in pure and doped vanadium dioxide. *Phys. Chem. Chem. Phys.* **2020**, *22*, 13474–13478.

(31) Lahnehan, D. J.; Slusar, T.; Beringer, D. B.; Jiang, H.; Kim, C.-Y.; Kim, H.-T.; Qazilbash, M. M. Insulator-to-metal transition in ultrathin rutile VO₂/TiO₂(001). *npj Quantum Materials* **2022**, *7*, 72.

(32) Lee, J.; Asheghi, M.; Goodson, K. E. Impact of thermoelectric phenomena on phase-change memory performance metrics and scaling. *Nanotechnology* **2012**, *23*, 205201.

(33) Suh, D.-S.; Kim, C.; Kim, K. H. P.; Kang, Y.-S.; Lee, T.-Y.; Khang, Y.; Park, T. S.; Yoon, Y.-G.; Im, J.; Ihm, J. Thermoelectric heating of Ge₂Sb₂Te₅ in phase change memory devices. *Appl. Phys. Lett.* **2010**, *96* (12), 123115.

(34) Zimmers, A.; Aigouy, L.; Mortier, M.; Sharoni, A.; Wang, S.; West, K. G.; Ramirez, J. G.; Schuller, I. K. Role of Thermal Heating on the Voltage Induced Insulator-Metal Transition in VO₂. *Phys. Rev. Lett.* **2013**, *110*, 056601.

(35) Kim, J.; Ko, C.; Frenzel, A.; Ramanathan, S.; Hoffman, J. E. Nanoscale imaging and control of resistance switching in VO₂ at room temperature. *Appl. Phys. Lett.* **2010**, *96*, 213106.

(36) Lin, J.; Ramanathan, S.; Guha, S. Electrically Driven Insulator–Metal Transition-Based Devices—Part I: The Electrothermal Model and Experimental Analysis for the DC Characteristics. *IEEE Trans. Electron Devices* **2018**, *65*, 3982–3988.

(37) Lin, J.; Ramanathan, S.; Guha, S. Electrically Driven Insulator–Metal Transition-Based Devices—Part II: Transient Characteristics. *IEEE Trans. Electron Devices* **2018**, *65*, 3989–3995.

(38) Li, D.; Sharma, A. A.; Gala, D. K.; Shukla, N.; Paik, H.; Datta, S.; Schlom, D. G.; Bain, J. A.; Skowronski, M. Joule Heating-Induced Metal–Insulator Transition in Epitaxial VO₂/TiO₂ Devices. *ACS Appl. Mater. Interfaces* **2016**, *8*, 12908–12914.

(39) Valmianski, I.; Wang, P. Y.; Wang, S.; Ramirez, J. G.; Guénon, S.; Schuller, I. K. Origin of the current-driven breakdown in vanadium oxides: Thermal versus electronic. *Phys. Rev. B* **2018**, *98*, 195144.

(40) Joushaghani, A.; Jeong, J.; Paradis, S.; Alain, D.; Stewart Aitchison, J.; Poon, J. K. S. Electronic and thermal effects in the insulator-metal phase transition in VO₂ nano-gap junctions. *Appl. Phys. Lett.* **2014**, *105*, 231904.

(41) Pergament, A.; Boriskov, P.; Velichko, A.; Kuldin, N. Switching effect and the metal–insulator transition in electric field. *J. Phys. Chem. Solids* **2010**, *71*, 874–879.

(42) Gopalakrishnan, G.; Ruzmetov, D.; Ramanathan, S. On the triggering mechanism for the metal–insulator transition in thin film VO₂ devices: electric field versus thermal effects. *J. Mater. Sci.* **2009**, *44*, 5345–5353.

(43) Simon Mun, B.; Yoon, J.; Mo, S.-K.; Chen, K.; Tamura, N.; Dejoie, C.; Kunz, M.; Liu, Z.; Park, C.; Moon, K.; Ju, H. Role of joule heating effect and bulk-surface phases in voltage-driven metal–insulator transition in VO₂ crystal. *Appl. Phys. Lett.* **2013**, *103*, 061902.

(44) Brockman, J. S.; Gao, L.; Hughes, B.; Rettner, C. T.; Samant, M. G.; Roche, K. P.; Parkin, S. S. P. Subnanosecond incubation times for electric-field-induced metallization of a correlated electron oxide. *Nat. Nanotechnol.* **2014**, *9*, 453–458.

(45) Yang, Z.; Hart, S.; Ko, C.; Yacoby, A.; Ramanathan, S. Studies on electric triggering of the metal–insulator transition in VO₂ thin films between 77 and 300 K. *J. Appl. Phys.* **2011**, *110*, 033725.

(46) Schroeder, H. Poole-Frenkel-effect as dominating current mechanism in thin oxide films—An illusion? *J. Appl. Phys.* **2015**, *117*, 215103.

(47) Ko, C.; Ramanathan, S. Observation of electric field-assisted phase transition in thin film vanadium oxide in a metal-oxide-semiconductor device geometry. *Appl. Phys. Lett.* **2008**, *93*, 252101.

(48) Ruzmetov, D.; Gopalakrishnan, G.; Deng, J.; Narayanamurti, V.; Ramanathan, S. Electrical triggering of metal–insulator transition in nanoscale vanadium oxide junctions. *J. Appl. Phys.* **2009**, *106*, 083702.

(49) Spitzig, A.; Pivonka, A.; Frenzel, A.; Kim, J.; Ko, C.; Zhou, Y.; Hudson, E.; Ramanathan, S.; Hoffman, J. E.; Hoffman, J. D. Nanoscale thermal imaging of VO₂ via Poole–Frenkel conduction. *Appl. Phys. Lett.* **2022**, *120*, 151602.

(50) Ganichev, S. D.; Ziemann, E.; Prettl, W.; Yassievich, I. N.; Istratov, A. A.; Weber, E. R. Distinction between the Poole-Frenkel and tunneling models of electric-field-stimulated carrier emission from deep levels in semiconductors. *Phys. Rev. B* **2000**, *61*, 10361–10365.

(51) Yamakawa, H.; Miyamoto, T.; Morimoto, T.; Terashige, T.; Yada, H.; Kida, N.; Suda, M.; Yamamoto, H. M.; Kato, R.; Miyagawa, K.; Kanoda, K.; Okamoto, H. Mott transition by an impulsive dielectric breakdown. *Nat. Mater.* **2017**, *16*, 1100–1105.

(52) Eckstein, M.; Oka, T.; Werner, P. Dielectric Breakdown of Mott Insulators in Dynamical Mean-Field Theory. *Phys. Rev. Lett.* **2010**, *105*, 146404.

(53) Heidrich-Meisner, F.; González, I.; Al-Hassanieh, K. A.; Feiguin, A. E.; Rozenberg, M. J.; Dagotto, E. Nonequilibrium electronic transport in a one-dimensional Mott insulator. *Phys. Rev. B* **2010**, *82*, 205110.

(54) Bohaichuk, S. M.; Muñoz Rojo, M.; Pitner, G.; McClellan, C. J.; Lian, F.; Li, J.; Jeong, J.; Samant, M. G.; Parkin, S. S. P.; Wong, H.-S. P.; Pop, E. Localized Triggering of the Insulator-Metal Transition in VO₂ Using a Single Carbon Nanotube. *ACS Nano* **2019**, *13*, 11070–11077.

(55) Zhang, Y.; Ramanathan, S. Analysis of “on” and “off” times for thermally driven VO₂ metal–insulator transition nanoscale switching devices. *Solid-State Electron.* **2011**, *62*, 161–164.

(56) El Abbassi, M.; Pósa, L.; Makk, P.; Nef, C.; Thodkar, K.; Halbritter, A.; Calame, M. From electroburning to sublimation: substrate and environmental effects in the electrical breakdown process of monolayer graphene. *Nanoscale* **2017**, *9*, 17312–17317.

(57) Hamaoui, G.; Horny, N.; Gomez-Heredia, C. L.; Ramirez-Rincon, J. A.; Ordonez-Miranda, J.; Champeaux, C.; Dumas-Bouchiat, F.; Alvarado-Gil, J. J.; Ezzahri, Y.; Joulain, K.; Chirtoc, M.

Thermophysical characterisation of VO₂ thin films hysteresis and its application in thermal rectification. *Sci. Rep.* **2019**, 9 (1), 8728.

(58) Hopkins, P. E. Thermal Transport across Solid Interfaces with Nanoscale Imperfections: Effects of Roughness, Disorder, Dislocations, and Bonding on Thermal Boundary Conductance. *ISRN Mech. Eng.* **2013**, 2013, 682586.

(59) Oh, D.-W.; Ko, C.; Ramanathan, S.; Cahill, D. G. Thermal conductivity and dynamic heat capacity across the metal-insulator transition in thin film VO₂. *Appl. Phys. Lett.* **2010**, 96, 151906.

(60) Santos, R.; Loureiro, J.; Nogueira, A.; Elangovan, E.; Pinto, J. V.; Veiga, J. P.; Busani, T.; Fortunato, E.; Martins, R.; Ferreira, I. Thermoelectric properties of V₂O₅ thin films deposited by thermal evaporation. *Appl. Surf. Sci.* **2013**, 282, 590–594.

(61) Wang, Q.; Liang, X.; Liu, B.; Song, Y.; Gao, G.; Xu, X. Thermal conductivity of V₂O₅ nanowires and their contact thermal conductance. *Nanoscale* **2020**, 12, 1138–1143.

(62) Kang, M.; Kim, S. W.; Ryu, J.-W.; Xu, Y.; Kato, R. Optical and thermal properties of V₂O₅ thin films with crystallization. *Journal of the Korean Physical Society* **2013**, 62, 1134–1138.

(63) Sheng, X.; Li, Z.; Cheng, Y. Electronic and Thermoelectric Properties of V₂O₅, MgV₂O₅, and CaV₂O₅. *Coatings* **2020**, 10, 453.